Filamentation and supercontinuum generation by singular beams in self-focusing nonlinear media

Georgi Maleshkov[1], Dragomir N. Neshev[2], Elitza Petrova[1], and Alexander Dreischuh[1,2]

[1]*Department of Quantum Electronics, Faculty of Physics, Sofia University "St. Kl. Ohridski", 1164 Sofia, Bulgaria*

[2]*Nonlinear Physics Centre and Center for Ultra-high bandwidth Devices for Optical Systems (CUDOS), Research School of Physics and Engineering, Australian National University, Canberra, ACT 0200, Australia*

(Dated: February 24, 2011)

We study numerically and experimentally the propagation of pulsed singular beams, including dark crosses and optical vortices, in self-focusing nonlinear media, resulting in filamentation and supercontinuum generation. Our results show that the singular beams survive the process of modulation instability and appear well preserved in both the near and far-field.

Keywords: singular beams, dark cross beams, optical vortex, self-focusing, filamentation

I. INTRODUCTION

The study of waves with spatial phase dislocations has became increasingly intriguing with the advent of various applications of singular beams, including particle micromanipulation [1], imaging [2], interferometry [3], and quantum information [4]. Phase dislocations in the wavefront of a beam determine its intensity structure, where at the dislocation line or point, the intensity vanishes. Important examples of beams with phase dislocation are the optical vortices (OVs) and the one-dimensional (1D) odd dark stripes. OVs are associated with an isolated point singularity with a 2π helical phase profile around, while the odd dark stripes contain π step-like phase dislocation along a line. Importantly, two or more dark stripes can be crossed in the transverse plane of the beam to form dark crosses (DCs) with flat phase distribution [5].

Phase dislocations also play an important role in nonlinear science, with notable examples of vortex filamentation [6, 7] and supercontinuum (SC) generation [8]. Nonlinear optics benefits greatly from the development of ultra-short-pulse laser sources due to their high peak intensities. However, encoding phase dislocation into pulsed beams with wide spectral bandwidth becomes a challenging task. In the case of short pulses with small spectral bandwidths, phase masks or computer generated holograms (CGHs) can create phase dislocations without the need for additional dispersion compensating elements [9]. In contrast, for sub-50-femtosecond laser-pulses with broad spectral bandwidth, special dispersion compensating techniques such as dispersionless $4f$ setups [10, 11], $2f - 2f$ setups [12, 13], double-pass gratings [14], or prism compressors [15] need to be employed. Other successful techniques make use of achromatic vortex lens [16], uniaxial crystals [17, 18], axially symmetric polarizers [19] or pair of closely spaced and parallel volume phase holographic gratings [20].

While the propagation of singular beams in self-defocusing nonlinear media (NLM) has been widely studied [21], their evolution in *self-focusing* NLM is less explored [22–24]. This is somewhat surprising because self-focusing materials are more common in nature, but it could be explained by the intrinsic azimuthal and modulation instabilities of the beams. While the process of vortex break-up resulting from such instabilities have been studied in the past [7, 25–27], the process of SC generation, that also stems from the self-focusing nonlinearity [28], has only recently been explored with OVs [8]. However, deeper understanding of the singular beam dynamics in such media is required to bring this process to practical importance.

Here we study numerically and experimentally the origin of filamentation and the subsequent SC generation of short laser pulses carrying DCs or OVs. We show that the trigger of the filamentation process in DCs is the amplitude modulation resulting from the hologram-to-NLM free space propagation. For the case of OVs, such filamentation pattern is only observed when weak azimuthal perturbations are included. Experimentally, we also observe that the propagation of the singular beams leads to the generation of ordered structures of hot-spots (filament patterns) that seed the SC white light generation. An important observation is that both the DCs and the OVs survive the modulation instability process and preserve their characteristic phase profiles.

II. NUMERICAL RESULTS

A. Model

As initial conditions we consider short Gaussian pulses with a DC on a super-Gaussian background beam or an OV imprinted on a Gaussian beam. The regime of propagation involves (i) free space propagation (from the CGH to the NLM), (ii) nonlinear evolution in the regime of dominating nonlinearity (inside the NLM), and (iii) free-space propagation to the plane of observation. The general model for pulsed-beam propagation in a nonlinear medium is based on the (3+1)D nonlinear Schrödinger equation for the slowly varying field envelope A,

$$i\frac{\partial A}{\partial z} - \frac{\beta}{2}\frac{\partial^2 A}{\partial t^2} + \frac{1}{2}\left(\frac{\partial^2}{\partial x^2} + \frac{\partial^2}{\partial y^2}\right)A + \frac{L_{\mathrm{Diff}}}{L_{\mathrm{NL}}}|A|^2 A = 0. \quad (1)$$

Here z and (x, y) are the normalized longitudinal and transverse coordinates, respectively. (x, y) are normalized to the dark beam widths w_0, while the longitudinal coordinate z is expressed in units of diffraction lengths $L_{\rm Diff} = kw_0^2$. In the above equation, $k = 2\pi n/\lambda$ with n being the refractive index of the NLM and λ - the wavelength of light in vacuum. $L_{\rm NL} = 1/(k|n_2|I)$ stands for the nonlinear length and $n_2 > 0$ is the self-focusing nonlinear Kerr coefficient. The intensity $I = |A|^2$ is normalized to the intensity needed to form a 1D dark soliton $I_{\rm sol}^{\rm 1D}$ in the case of defocusing nonlinearity ($n_2 < 0$).

Because in our experiment we use 150 fs pulses and short (5 mm) NLM, the dispersion length inside the NLM (~ 75 cm) is much longer as compared to both the diffraction and nonlinear lengths (and to the length of the NLM itself). Therefore, we can assume that the pulse profile does not change inside the medium, hence we can treat the time coordinate as a parameter in our model. While the pulse shape can change at high enough nonlinearity even with weak dispersion [29], this is not the case in our experiments with moderate pulse peak powers. As such, the filamentation process is closely linked to the spatial modulation instability of the beam, without a complete spatiotemporal collapse of the filaments [30]. In this case, Eq. (1) can be reduced to an effective (2+1)D model.

In order to account for the time variation of the pulse, we assume a Gaussian pulse of width t_0 and divide it into $4N$ time slices, each one having duration $\tau_{slice} = t_0/N$. The total beam intensity distribution is then calculated as a time-integrated picture over all $4N$ slices. The total slice number used in the simulations ($N = 64$) is determined from the energy conservation and the reproducibility of the transverse intensity distribution in the time-integrated picture against doubling the number of slices. We note that Eq. (1), with a time coordinate treated as a parameter, does not describe the true process of SC generation, however provides a clear description of the initial stages of self-focusing and hot-spots generation that are precursors for the continuum generation.

The input DC beam is modeled by

$$A(r, \theta, t) = A_0 C(t) B(r) \tanh(r\cos\theta/w_0) \tanh(r\sin\theta/w_0), \tag{2}$$

with $\theta = 45°$, while the OV is described by [31]

$$A(r, \theta, t) = A_0 C(t) B_1(r)(r/w_0)^{|m|} \exp(im\theta), \tag{3}$$

where $r = \sqrt{x^2 + y^2}$, θ, and t are the radial, azimuthal, and time coordinates, respectively. m is OV topological charge. $B(r) = \exp[-(r/r_0)^{14}]$, and $B_1(r) = \exp[-(r/w_0)^2]$ describe the super-Gaussian and Gaussian bright background beams, respectively. $C(t) = \exp[-(t/t_0)^2]$ is the pulse temporal profile. The initial intensity and phase profiles of both singular beams at local time $t = 0$ (at the pulse peak) are shown in Fig. 1.

In a real experiment these initial profiles are perturbed by experimental noise that can trigger the instabilities. While such noise is specific to each particular experiment,

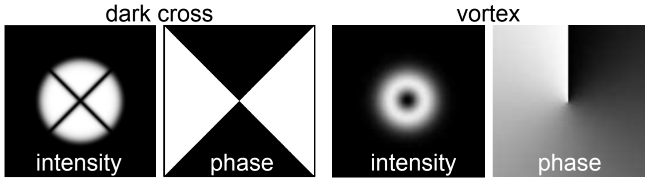

FIG. 1: Intensity and phase profiles of DC beam (left) and an unperturbed OV $m = 1$ (right) at $t = 0$.

for simplicity we consider initial (at z=0) periodic azimuthal perturbation,

$$A_p(r, \theta, t) = A(r, \theta, t)[1 + \delta\cos(\kappa\theta)], \tag{4}$$

where κ is the integer azimuthal wavenumber and $A(r, \theta, 0, t)$ is given by Eq. (3). We note that even though such perturbation is far from the realistic experimental conditions it helps to capture the important qualitative characteristics of the instability process.

For the case of DCs, the background beam oscillations induced during the free-space propagation from the CGH to the NLM are sufficient for initiating the beam's modulation instability. Other perturbations can only enrich the instability patterns, but are not prerequisite. For our numerical simulations we use beam propagation method, where for each time slice we use a computational grid of 1024×1024 points. The total beam energy density distribution is calculated as time-integrated picture from all 256 temporal slices.

We first discuss the numerical results for the propagation of DCs, followed by the results on the azimuthally perturbed OVs. In order to keep the slowly varying amplitude envelope approximation, under which Eq. (1) is valid, in the numerical calculations we restrict the input background beam intensity and the length of the NLM such that the maximum output intensity of the central temporal slice with the self-focusing hot spots remains always below $20I_{sol}^{1D}$. In the presented numerical simulations of propagation of DCs, the NLM length is $1.6L_{\rm Diff}$ and the initial peak intensity of the central temporal slice is in the range $[0.6-0.8]I_{sol}^{1D}$. In order to match the maximum OV beam intensity to I_{sol}^{1D} we take $A_0 = 1.474$. However, only after increasing the field amplitude by a factor of 2, a well pronounced bright vortex ring self-focusing is clearly seen at $z = 6L_{\rm Diff}$. In all cases of OVs we use initial modulation $\delta = 0.05$ [see Eq. (4)].

B. Dark crosses

To examine in details the evolution of the DCs inside the NLM, we first perform numerical simulations. Here we change the position of the nonlinear media only (with steps of $2L_{\rm Diff}$), while keeping its length and all other initial parameters unchanged. These simulations give us the opportunity to vary the free-space propagation from the CGH to the NLM, which is needed to separate the first-order diffracted beam from the CGH with the DC

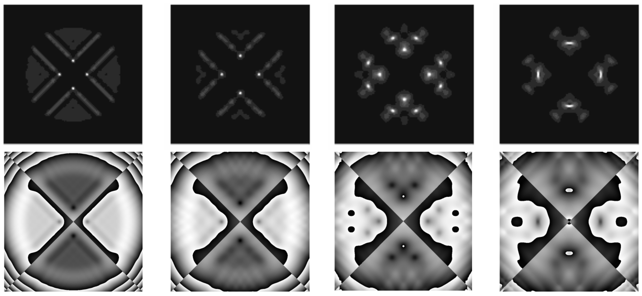

FIG. 2: Intensity (upper row) and phase profiles (lower row) of the DC central temporal slice at the exit of the NLM. The NLM is placed at $1.65L_{\mathrm{Diff}}$ (first column), $4L_{\mathrm{Diff}}$ (second column), $8L_{\mathrm{Diff}}$ (third column) and at $12L_{\mathrm{Diff}}$ (last column) behind the CGH. The normalized initial intensity of the central temporal slice is $I(t=0)/I_{sol}^{1D}=0.6$. The length of the NLM is $1.6L_{\mathrm{Diff}}$. 51% of the total computational area are shown.

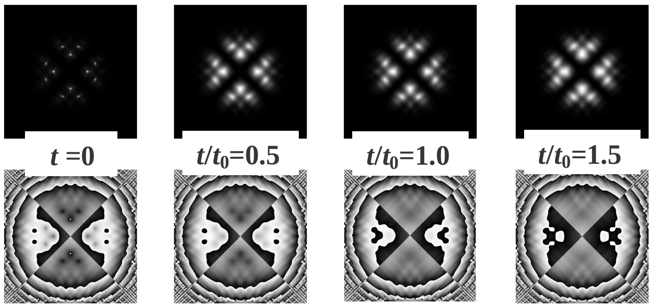

FIG. 3: Normalised intensity (upper row) and phase profiles (lower row) of the DCs at the exit of the NLM located at $8L_{\mathrm{Diff}}$ for local times (left to right) $t/t_0=0, 0.5, 1.0$, and 1.5. $I(t=0)/I_{sol}^{1D}=0.75$. The length of the NLM is $1.6L_{\mathrm{Diff}}$. 34% of the total computational area are shown.

nested in. Experimentally, this is analogous to translating the 5 mm thick CaF_2 sample with respect to the focusing lens. In Fig. 2 we present the evolution of the central temporal slice of the pulse for different positions of the NLM. When the initial free-space propagation is relatively short, e.g. $1.65L_{\mathrm{Diff}}$, the central hot spots are dominating, whereas the satellites almost do not differ from the background. Increasing the initial propagation distance to the NLM, the satellite hot spots become more intense. By increasing the CGH-to-NLM free space propagation distance up to $8L_{\mathrm{Diff}}$ (third frame in Fig. 2), the sub-structure of the beam changes - the satellite hot spots become more intense than the central (initial) ones. Increasing the distance further (up to $12L_{\mathrm{Diff}}$) the beam changes again – the satellite hot spots diffract stronger and the nonlinearity forces the central hot spots to dominate again (last frame in Fig. 2).

Next, we examine the profiles of the DCs at different local times within the pulse envelope (i.e. at different intensities) at the exit of the NLM, when the initial free-space propagation is $8L_{\mathrm{Diff}}$. In this case we have relatively strong satellite hot spots (see Fig. 2). The obtained numerical results are shown in Fig. 3. As expected, the decrease of the beam intensity at longer local times, in the pulse wings, results in weaker confinement

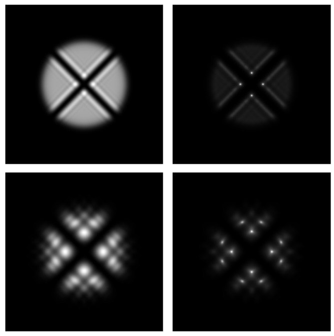

FIG. 4: Time-integrated energy density profiles of DCs at the entrance (top row) and at the exit of the NLM (bottom row) for a NLM located at $1.6L_{\mathrm{Diff}}$ (left) and $8L_{\mathrm{Diff}}$ (right). The length of the NLM is $1.6L_{\mathrm{Diff}}$. 34% of the total computational area are shown.

of the bright sub-beams. Because all frames are normalised to the maximum intensity in the frame, the image with the strongest focused filaments (left upper frame in Fig. 3) appears darkest. We note that despite the nonlinear phase modulation, the step-like phase dislocations of π along the two crossed dark lines are present in each time slice, i.e. for each local intensity within the pulse envelope. Hence, the DCs should survive the entire pulsed beam filamentation and should be also present in the time-integrated energy-density distribution of the beam. This is shown in Fig. 4 for two different free-space propagation distances. As seen, an easy way to control the relative intensity of the self-focused satellite sub-beams with respect to the central ones is by changing the free-space propagation to the NLM.

C. Optical vortices

Next we study the dynamics of an OV inside the NLM and we focus on charge-one OVs ($m=1$). Under perfect numerical conditions (no azimuthal perturbation) and sufficiently high input beam intensity, we observe shrinking of the bright vortex ring without any vortex break-up. The azimuthal instability, however is clearly seen when we impose an initial azimuthal amplitude perturbation [Eq. 4] onto the bright OV ring. In this case, each perturbed time slice evolves in a different manner in space inside the NLM due to its different local intensity. While in the peak of the pulse (at a local time $t=0$) we have vividly pronounced break-up of the vortex beam into hot spots, at lower intensities (in the pulse wings), we see weaker modulation instability (decay in lower number of sub-beams rotating at different angles for the different pulse intensities). For four azimuthal modulation periods ($\kappa=4$) we observe symmetric decay of the vortex ring into four sub-beams (not shown) that self-focus (at sufficiently high intensity $I(t=0)/I_{sol}^{1D}=2.2-4$), repel each other and rotate as an ordered structure.

A better match with the experimental observations (see Sec. III) is achieved in the case of an amplitude az-

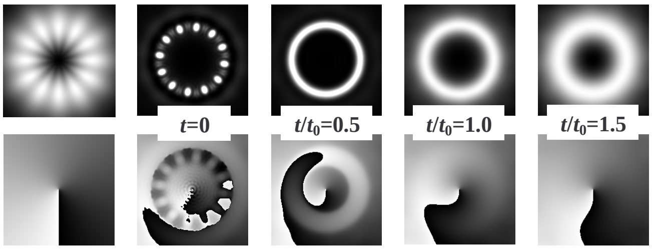

FIG. 5: Normalized intensity (upper row) and phase profiles (lower row) of the azimuthally perturbed vortex ring ($\kappa = 12$, left column) and the intensity profiles at the exit of the NLM at local times (left to right) $t/t_0 = 0, 0.5, 1.0$, and 1.5. Note that the spiral phase profile is present in each time slice. $I(t = 0)/I_{sol}^{1D} = 0.8$ and $z/L_{\text{Diff}} = 0.375$. Some 3.8% of the total computational area are shown in each frame.

imuthal perturbation of 12 periods ($\kappa = 12$, upper left frame in Fig. 5). In this case, the input vortex ring is 4 times wider as compared to the vortex ring in Fig. 1. The peak intensity is $I(t = 0)/I_{sol}^{1D} = 0.8$ and the nonlinear propagation is $z = 0.375L_{\text{Diff}}$. At high intensity the azimuthal perturbation forces the vortex ring to decay into axially-symmetric set of 12 sub-beams (Fig. 5, frame at $t = 0$). The decrease of the local intensity (at increased local times) decreases the growth-rate of the instability and the OV experiences weaker and weaker self-focusing, approaching the regime of linear diffraction far in the leading and trailing edges of the pulse. This tendency is clearly seen in Fig. 5. Note that despite the nonlinear vortex ring beak-up, the helical 2π phase profile and the point phase dislocation are present at all local times within the pulse envelope. Hence, the OVs survive the filamentation instability process and should be present in the time-integrated energy-density distribution.

The numerical results shown in Fig. 6 clearly demonstrate this behavior, both at the exit of the NLM (left) and after linear propagation distance $z = 1.125L_{\text{Diff}}$ behind the NLM (right images). The left image in Fig. 6 corresponds to the data in Fig. 5 and presents the time-integrated energy-density distribution in the case of 12 periods of 5% initial azimuthal perturbation. It is important to note that, in an agreement with the experiment, OVs fully recover after relatively short free-space propagation distance (see Fig. 6, right image). If we intentionally saturate right image in Fig. 6, one can also see the broad background caused by the diffracting self-focused filaments, which is only intuitively reminiscent of the SC white light seen in the experiment [8].

III. EXPERIMENTAL RESULTS

A. Experimental setup

In our experiments we first imprint an OV or a a DC onto an intense pulsed background beam and then study the process of hot spot formation in a bulk NLM. Our experimental setup is similar to the one recently used

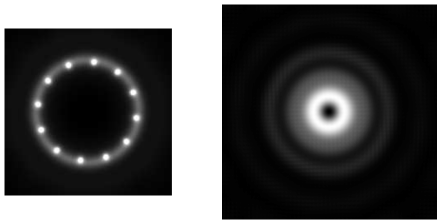

FIG. 6: Time-integrated pictures of OVs for $\kappa = 12$ for $I(t = 0)/I_{sol}^{1D} = 0.8$. Left: at the exit of the NLM; Right: after free-space propagation of $z = 1.125L_{\text{Diff}}$ behind the NLM.

in Ref. [8]. We utilize a 250 Hz repetition rate chirped-pulse amplification system (CPA-2001, Clark-MXR Inc.) delivering 150 fs pulses and peak power of 15 MW, at a central wavelength of 775 nm. For DCs and OVs generation, we use a CGH, fabricated by etching the respective interference pattern onto a glass substrate. The efficiency of the holograms is $\sim 30\%$, and the large grating period of 80 μm was found to cause negligible chromatic dispersion over the pulse bandwidth. An iris diaphragm, located about 100 cm behind the CGH and 200 cm in front of the focusing lens, is used to select the singular dark beam formed in the first diffraction order of the hologram. The beam polarization state can be controlled by a $\lambda/4$ waveplate. The NLM is 5 mm thick CaF_2 crystal that is continuously rotated in order to prevent possible damage due to thermal effects.

In order to smoothly control the beam intensity inside the NLM, we vary the position of the beam waist with respect to the CaF_2 sample, keeping the sample-to-imaging lens distance unchanged. The data acquisition system consists of a color CCD camera and a fiber-optic spectrometer. Our experimental setup allows for simultaneous measurements of the field intensity profiles at the output of the medium and the far-field intensity distribution (Fourier domain).

B. Dark cross beams

We monitor the evolution of the DCs in both near (Fig. 7) and far field with increasing beam intensity (i.e. by changing the focusing lens-to-sample distance). As indicated in our numerical simulations (Figs. 3, 4) the beam diffraction from the CGH to the NLM causes background-beam oscillations parallel to the dark stripes (Fig. 7, upper row). These appear as natural precursors for the filamentation in the high-power regime as seen in Fig. 7(lower row). In agreement with the numerical simulations, well preserved DCs are observed in both near- and far-field.

At high laser powers, the beam generates bright SC, which spectrum is shown in Fig. 8 together with the spectrum of the initial laser pulse. The output profiles of the SC is recorded in our experiment on a color CCD camera. An interesting observation can be made at the initial stage of the SC generation when (vibrating) interference fringes and lattices can be seen with both OVs

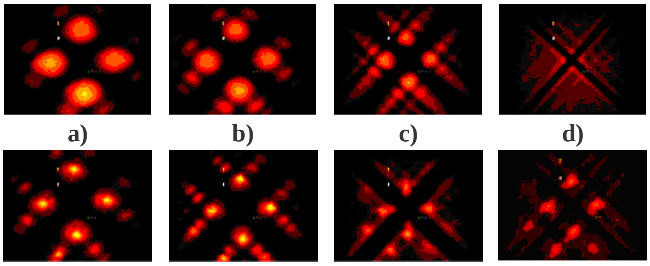

FIG. 7: Near-field DCs observed for low power (upper row, 0.5 mW) and high power (bottom row, 15 mW) at decreasing focusing lens-to-sample distance: (a) 3 mm, (b) 2 mm, (c) 1 mm, and (d) 0 mm. In case (d) clear filamentation is observed above 6 mW. Each frame is 360 μm wide.

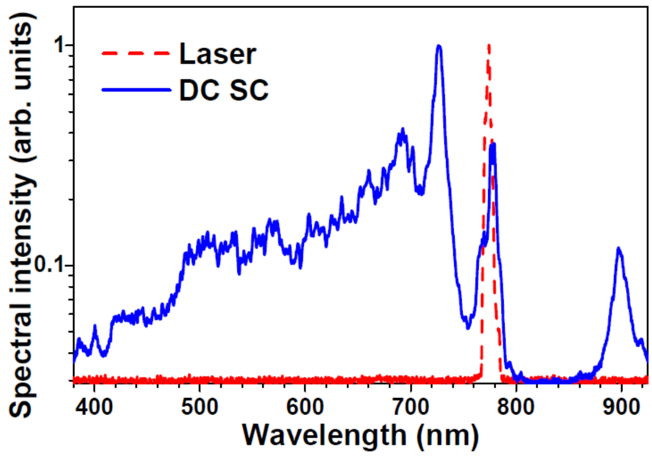

FIG. 8: Spectra of the SC generated in CaF_2 at $P = 15$ mW (solid curve) and the laser source (dashed curve).

and DCs. We attribute these structures to interference of coherent supercontinua generated from different (but low in number) hot spots. The observed tendency is that the brighter the SC, the lower the visibility of the interference structures. The visibility of the interference patterns seen at high-power ($\sim 6 - 8$ mW) however is better with DCs due to the well defined number of filaments. In Fig. 9 we show experimental picture of the typical interference lines. For better visualization, in the left frame we have slightly adjusted the intensity of the red components, whereas in the right frame we show the same, but in inverted colors, for better visibility.

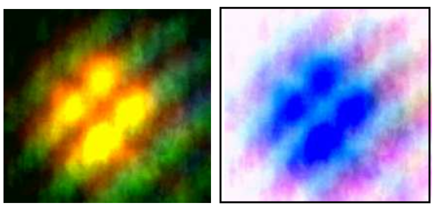

FIG. 9: Far-field of the DC with generated white-light interference fringes, at a power near the SC generation threshold. Left - image with slightly adjusted intensity of the red components; right - the same, but in inverted colors.

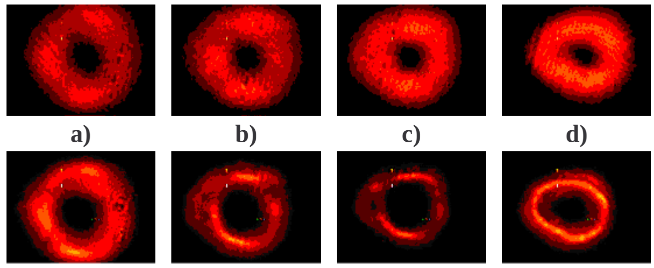

FIG. 10: Near-field OV rings observed for low power (upper row) and vortex ring self-focusing and hot spots formation for high power (bottom row; 22 mW average power) at decreasing focusing lens-to-sample distance: a) 3 mm; b) 2 mm; c) 1 mm; d) 0 mm. In case d) SC generation starts at 8 mW. Full horizontal scale of each frame is 360 μm.

C. Optical vortices

When OVs are focused inside the CaF_2 sample, again we see the generation of a broad SC (in the far-field) above a certain power threshold. The SC does not carry any phase singularities and appears as an incoherent superposition of a large number of continua that are triggered by the individual hot spots. Similar to the SC generated from DCs, near the SC threshold, unstable interference fringes can be seen in different colors. However, in the far field we always observe a well preserved OV beam in the background of the generated SC.

The origin of the SC was clarified by inspecting the transverse near-field intensity distribution of the pump beam at the exit of the sample. In Fig. 10 we show a comparison between the low power (upper row) and high power (22 mW average power, bottom row) OV intensity distribution. In the linear regime (upper row), it can be seen how the OV becomes focused with decreasing the focusing lens-to-sample distance. In the nonlinear regime (bottom row), the vortex ring is shrinking and self-focusing but is well pronounced and is accompanied by increasing [from (a) to (c)] number of hot spots in the beam. These hot spots generate the SC radiation which, because of its much stronger diffraction after the exit of the NLM, appears in the far-field as a white-light background for the vortex. In agreement with our numerical simulations (Fig. 6, left), the hot spots appear arranged along the vortex ring, i.e. at the positions of high local peak intensity. Despite some deformation, the symmetry of the OV as well as the OV core remain well preserved.

IV. CONCLUSIONS

Numerical simulations carried out on the base of the (2+1)-dimensional nonlinear Schrödinger equation, treating the time as a parameter, showed that at high intensities of the femtosecond pulses, the dark crosses and optical vortices undergo self-focusing and formation of multiple hot spots due to the modulation instability. These hot spots trigger, in real experimental situation, SC generation. We experimentally demonstrate femtosecond SC generation in a bulk nonlinear medium by OVs and DCs. The results show that the spatial profiles of the DCs and the OVs remain well preserved in the process of SC generation. However, the generated continuum appears as a white-light background surrounding the fundamental singular beams. We have deducted that strong diffraction of the SC generated from each filament is the reason for the observed white-light background. Near the threshold for SC generation, a low number of hot spots can generate several continua that interfere, resulting in pronounced interference patterns for certain spectral components. However, when a large number of colorred self-focusing sub-beams are created, the specific phases of the DCs and the OV beam are not transferred into the SC spatial profile, likely due to the initial noise on the initial singular optical beams.

V. ACKNOWLEDGMENTS

The authors thank Yu. S. Kivshar for the useful discussions and M. Sammoc for help with the experiments. This work was supported by the Science Fund of the Sofia University (grant 128/2009), by the NSF-Bulgaria (grants DO-02-0114/2008 and IRNI-17/2007), and by the Australian Research Council.

---

[1] D. G. Grier, Nature **424**, 810 (2003).
[2] G. Foo, D. M. Palacios, and G. A. Swartzlander, Jr., Opt. Lett. **30**, 3308 (2005).
[3] S. Furhapter, A. Jesacher, S. Bernet, and M. Ritsch Marte, Opt. Lett. **30**, 1953 (2005).
[4] G. Molina-Terriza, J. P. Torres, and L. Torner, Nat. Physics **3**, 305 (2007).
[5] G. A. Swartzlander, Jr., D. R. Andersen, J. J. Regan, H. Yin, and A. E. Kaplan, Phys. Rev. Lett. **66**, 1583 (1991).
[6] A. Vinçotte and L. Bergé, Phys. Rev. Lett. **95**, 193901 (2005).
[7] L. T. Vuong, T. D. Grow, A. Ishaaya, A. L. Gaeta, G. W. 't Hooft, E. R. Eliel, and G. Fibich, Phys. Rev. Lett. **96,** 133901 (2006).
[8] D. N. Neshev, A. Dreischuh, G. Maleshkov, M. Samoc, and Yu. S. Kivshar, Opt. Express **31**, 18368 (2010).
[9] K. J. Moh, X.-C. Yuan, D. Y. Tang, W. C. Cheong, L. S. Zhang, D. K. Y. Low, X. Peng, H. B. Niu, and Z. Y. Lin, Appl. Phys. Lett. **88**, 091103 (2006).
[10] K. Besuchanov, A. Dreischuh, M. G. Schätzel, G.G. Paulus, and H. Walther, Opt. Lett. **29**, 1942 (2004).
[11] I. Zeylikovich, H. I. Sztul, V. Kartazaev, T. Le, and R. R. Alfano, Opt. Lett. **32**, 2025 (2007).
[12] I. G. Mariyenko, J. Strohaber, and C. J. G. J. Uiterwaal, Opt. Express **13**, 7599 (2005).
[13] J. Strohaber, T. Scarborough, and C. J. G. J. Uiterwaal, Appl. Optics **46**, 8583 (2007).
[14] K. Besuchanov, A. Dreischuh, G. G. Paulus, M. G. Schätzel, H. Walther, D. Neshev, W. Krolikowski, and Yu. Kivshar, J. Opt. Soc. Am. B **23**, 26 (2006).
[15] A. Schwarz and W. Rudolph, Opt. Lett. **33**, 2970 (2008).
[16] G. A. Swartzlander, Jr., Opt. Lett. **31**, 2042–2044 (2006).
[17] A. Volyar, V. Shvedov, T. Fadeyeva, A. S. Desyatnikov, D. N. Neshev, W. Krolikowski, and Yu. S. Kivshar, Opt. Express **14**, 3724–3729 (2006).
[18] D. N. Neshev, A. Dreischuh, V. Shvedov, A. S. Desyatnikov, W. Krolikowski, and Yu. S. Kivshar, Opt. Lett. **33**, 1851–1853 (2008).
[19] Yu. Tokizane, K. Oka, and R. Morita, Opt. Express **17**, 14517–14525 (2009).
[20] O. Martínez-Matos, J. A. Rodrigo, M. P. Hernandez-Garay, J. G. Izquierdo, R. Weigand, M. L. Calvo, P. Cheben, P. Vaveliuk, and L. Banares, Opt. Lett. **35**, 652–654 (2010).
[21] A. S. Desyatnikov, Yu. S. Kivshar, and L. Torner, Prog. Optics **47**, 291 (2005).
[22] P. Hansinger, A. Dreischuh, G. G. Paulus, Opt. Commun. **282**, 3349 (2009).
[23] G. Maleshkov, D. N. Neshev, A. Dreischuh, Proc. SPIE **7501**, 75010G (2009).
[24] G. Maleshkov, D. N. Neshev, A. Dreischuh, Phys. Rev. A **80**, 053828 (2009).
[25] V. Tikhonenko, J. Christou, and B. Luther-Daves, J. Opt. Soc. Am. B **12**, 2046 (1995).
[26] W. J. Firth and D. V. Skryabin, Phys. Rev. Lett. **79**, 2450 (1997).
[27] L. Torner and D. V. Petrov, Electron. Lett. **33**, 608 (1997).
[28] R. R. Alfano and S. L. Shapiro, Phys. Rev. Lett. **24**, 584 (1970).
[29] A. Couairon, and A. Mysyrowicz, Phys. Rep. **441**, 47 (2007).
[30] M. A. Porras, A. Parola, D. Faccio, A. Couairon, and P. Di Trapani, Phys. Rev. A **76**, 011803 (2007).
[31] D. Rozas, C. T. Law, and G. A. Swartzlander, Jr., J. Opt. Soc. Am. B **14**, 3054 (1997).